

FULL PAPER

Open Access



# Reversible flowering of CuO nanoclusters via conversion reaction for dual-ion Li metal batteries

Siying Li<sup>1,2†</sup>, Jung-Hun Lee<sup>2†</sup>, Soo Min Hwang<sup>2\*</sup> and Young-Jun Kim<sup>2,3\*</sup> 

## Abstract

Dual-ion Li metal batteries based on non-flammable  $\text{SO}_2$ -in-salt inorganic electrolytes (Li- $\text{SO}_2$  batteries) offer high safety and energy density. The use of cupric oxide (CuO) as a self-activating cathode material achieves a high specific capacity with cost-effective manufacturing in Li- $\text{SO}_2$  batteries, but its cycle retention performance deteriorates owing to the significant morphological changes of the cathode active materials. Herein, we report the catalytic effect of carbonaceous materials used in the cathode material of Li- $\text{SO}_2$  batteries, which act as templates to help recrystallize the active materials in the activation and conversion reactions. We found that the combination of oxidative-cyclized polyacrylonitrile (PAN) with N-doped carbonaceous materials and multi-yolk-shell CuO (MYS-CuO) nanoclusters as cathode active materials can significantly increase the specific capacity to  $315.9 \text{ mAh g}^{-1}$  (93.8% of the theoretical value) at 0.2 C, which corresponds to an energy density of  $1295 \text{ Wh kg}_{\text{CuO}}^{-1}$ , with a capacity retention of 84.46% at the 200th cycle, and the cathode exhibited an atypical blossom-like morphological change.

**Keywords** Non-flammable,  $\text{SO}_2$ -in-salts electrolyte, Cupric oxide, Nano-structuring, Polyacrylonitrile, Conversion reaction

## 1 Introduction

Recently, the progress in Li-ion batteries (LIBs) has led to the development of new devices such as electric vehicles, mobile communication devices, and energy storage systems. These devices require high energy densities and long lifespans of LIBs. However, LIBs with organic electrolytes still present safety concerns as they can catch fire

or explosion because of the high flammability of their electrolytes. Moreover, next-generation high-energy-density rechargeable batteries such as Li-S and Li-air batteries present similar safety issues because they use flammable organic electrolytes [1, 2].

In 2015, Jeong et al. revisited inorganic  $\text{SO}_2$ -in-salt electrolytes and promoted the development of next-generation Li or Na secondary batteries with  $\text{SO}_2$ -in-salt electrolytes [3]. The ionic conductivity and flammability of  $\text{SO}_2$ -in-salt electrolytes comprising lithium or sodium tetrachloroaluminate ( $\text{LiAlCl}_4$  or  $\text{NaAlCl}_4$ , respectively) dissolved in liquid  $\text{SO}_2$  are higher and lower, respectively than those of conventional organic electrolytes [4–6]. Copper(II) chloride ( $\text{CuCl}_2$ ) has been used as a cathode material for  $\text{SO}_2$ -in-salt battery systems because it is inexpensive and its high specific capacity is comparable to that of the current LIB cathode materials [7, 8]. In addition, the voltage difference between the discharge and charge curves ( $\Delta V$ ) for the  $\text{CuCl}_2$ -to- $\text{CuCl}$  phase

<sup>†</sup>Siying Li and Jung-Hun Lee contributed equally to this work

\*Correspondence:

Soo Min Hwang  
smhwang@skku.edu

Young-Jun Kim  
yjkim68@skku.edu

<sup>1</sup> School of Mechanical and Automotive Engineering, Guangxi University of Science and Technology, Liuzhou 545616, China

<sup>2</sup> SKKU Advanced Institute of Nanotechnology (SAINT), Sungkyunkwan University, Suwon 16419, Republic of Korea

<sup>3</sup> SKKU Institute of Energy Science and Technology (SIEST), Sungkyunkwan University, Suwon 16419, Republic of Korea

transition in  $\text{SO}_2$ -in-salt secondary battery systems is negligible (approximately 0.11 V at 0.25 C) compared with those of other battery systems [7]. Although the energy density of  $\text{CuCl}_2$  cathodes ( $\sim 580 \text{ Wh kg}^{-1}$ ) and voltage efficiency during charging-discharging are high, their commercialization is hindered by their high moisture reactivity. To address this issue, Kwak et al., Kim et al., and Li et al. used copper metal and copper oxides as cathode materials, which were converted to  $\text{CuCl}$  or  $\text{CuCl}_2$  through a self-activation process before the initial charging or discharging began [9–11]. However, the self-activation process leads to a large volume expansion of the cathode (e.g., conversion of  $\text{CuO}$  to  $\text{CuCl}_2$  is accompanied by 224% volume expansion), which is responsible for the low initial capacity and degraded cycle retention of copper metal or copper oxide cathodes [10, 11].

To date, numerous researchers have focused on nanoengineering conversion-type active materials for rechargeable batteries [12–14]. Nanoengineering methods can be classified into four categories: downsizing, forming hollow or hierarchical structures, and hybridization with nanoscale carbonaceous materials [13]. Nano-sized active materials exhibit excellent electrochemical performance owing to their large surface areas and short  $\text{Li}^+$  ion diffusion lengths, facilitating fast charging [15–18]. Furthermore, the hollow structure can effectively alleviate the stress caused by volume changes by providing adequate space [19–22]. The structures developed by combining the advantages of the two aforementioned nanoengineering methods present a hierarchical configuration. In addition, such structures were hybridized with carbonaceous materials to provide smooth electron transfer pathways [23, 24]. Moreover, the crystallographic orientation of the active materials can be tuned using the carbon coating utilized as the template [25]. These methods can be used to develop Cu-based self-activating cathodes in  $\text{SO}_2$ -in-salt secondary batteries. Kwak et al. evaluated the performance of copper(I) oxide ( $\text{Cu}_2\text{O}$ ) with several nanostructures including mesoporous nanospheres, nanocubes, and nano-octahedrons [9]. Copper(II) oxide ( $\text{CuO}$ ) with nano- and microstructures as cathode materials in  $\text{SO}_2$ -in-salt secondary battery systems has been studied as well [11]. They reported that nanostructuring improved the specific capacity but did not affect the cycling performance of the cathodes because the active cathode material underwent significant micro-shape changes in addition to volume changes during cycling. Therefore, new methods are required to develop Cu-based cathodes with high energy densities and cycling stabilities for  $\text{SO}_2$ -in-salt secondary batteries.

Herein, we developed a hybrid nanoengineering-based method to fabricate high-performance cathodes for  $\text{SO}_2$ -in-salt secondary battery systems. As the cathode

material, multi-yolk-shell  $\text{CuO}$  (MYS- $\text{CuO}$ ), with a microsphere structure wrapped with nanoparticle clusters, was coated with cyclized polyacrylonitrile (PAN) and 0-D ketjen black (KB) as the conducting agent. The self-activation and charge-discharge reactions of the active materials were influenced by their initial morphology and the coated cyclized PAN and conducting KB, leading to interesting morphological changes and enhanced electrochemical properties. The reversible specific capacity of the cathode reached a high value of  $315.9 \text{ mAh g}^{-1}$  (93.8% of the theoretical value) at 0.2 C (1 C =  $300 \text{ mAh g}^{-1}$  for  $\text{CuO}$ ) and remarkable capacity retention of 84.46% at the 200th cycle. We believe that our results will promote the commercialization of Li metal dual-ion batteries with non-flammable  $\text{SO}_2$ -in-salt inorganic electrolytes.

## 2 Methods/experimental

### 2.1 Materials

Copper (II) acetate monohydrate ( $\text{Cu}(\text{CH}_3\text{COO})_2 \cdot \text{H}_2\text{O}$ , 98.0–102.0%), sodium hydroxide ( $\text{NaOH}$ , 98%) from Alfa Aesar, and L-ascorbic acid from Sigma-Aldrich were used for the fabrication (MYS- $\text{CuO}$ ). Lithium chloride ( $\text{LiCl}$ , 99.9%, ultra-dry), aluminum chloride ( $\text{AlCl}_3$ , 99.99%, ultra-dry), from Alfa Aesar, and sulfur dioxide ( $\text{SO}_2$ , 99.5%) purchased from Alpha Gas were used for  $\text{LiAlCl}_4 \cdot 3\text{SO}_2$  preparation. Poly(tetrafluoroethylene) (PTFE, 60 wt% emulsion in  $\text{H}_2\text{O}$ ) and polyacrylonitrile (PAN, Mw 150,000) from Sigma-Aldrich, 1-Methyl-2-pyrrolidone (NMP, 99.5%) from Samchun Chemicals, and Ketjen Black (KB, EC-600JD carbon black) from Akzo Nobel, Japan, were used for cathode fabrication. Glass microfiber (GF, 190  $\mu\text{m}$  thickness, GC50) obtained from Advantec was used as the separator. Thionyl chloride ( $\text{SOCl}_2$ , >99.5%) was purchased from Daejung Chemicals to wash out the  $\text{LiAlCl}_4 \cdot 3\text{SO}_2$  electrolyte remaining on the electrode after disassembling the cell.

### 2.2 Preparation of multi-yolk-shell $\text{CuO}$ microspheres

Multi-yolk-shell  $\text{CuO}$  microspheres (MYS- $\text{CuO}$ ) were used as the active materials. Mesoporous  $\text{Cu}_2\text{O}$  microspheres were then fabricated.  $\text{NaOH}$  pellets were dissolved in 165.6 mL deionized water to make the solution pH 11.3. The solution turned light blue when 50.4 mL of  $0.3 \text{ mol L}^{-1} \text{ Cu}(\text{CH}_3\text{COO})_2$  aqueous solution was added to the solution under stirring at 400 rpm. With the drop-wise addition of 54.0 mL of  $0.28 \text{ mol L}^{-1}$  ascorbic acid (AA) aqueous solution, the solution first changed to a brown turbid solution, and the suspension became yellow and saffron, revealing the formation of  $\text{Cu}_2\text{O}$  mesoporous microspheres. The mixture was stirred at room temperature for 20 min, collected, and washed with deionized water and ethanol via vacuum filtration. The saffron

powders were dried overnight in an 80 °C vacuum oven, followed by calcination at 360 °C for 10 h in a box furnace to obtain MYS-CuO. During the heat treatment of mesoporous Cu<sub>2</sub>O in air, the outward diffusion of copper atoms was faster than the inward diffusion of oxygen atoms, resulting in the hollow structure of CuO as a calcination product.

### 2.3 Preparation of SO<sub>2</sub>-in-salt electrolyte

AlCl<sub>3</sub> was stored in an Ar-filled ampule without further purification. The LiCl was dried in a vacuum oven at 120 °C for 24 h before use. AlCl<sub>3</sub> and LiCl were mixed at a molar ratio of 1:1.1 and sealed in a glass/Teflon vessel in an Ar gas-filled glove box (<1 ppm H<sub>2</sub>O and O<sub>2</sub>). An additional 10 mol% of LiCl was added to mitigate the formation of free AlCl<sub>3</sub>, which is corrosive to metals. SO<sub>2</sub> gas was blown into the vessel at a pressure of 1.5 bar. Subsequently, the white powder mixture became a transparent light-ochre-colored liquid. The SO<sub>2</sub> concentration was determined by weighing the vessel before and after SO<sub>2</sub> blowing. Finally, the fabricated electrolyte was transferred to a pre-vacuum-dried glass vial (120 °C, 24 h) in a humidity-controlled Ar gas-filled glove box (<1 ppm H<sub>2</sub>O and O<sub>2</sub>). A small piece of Li metal was added to the electrolyte to remove the AlCl<sub>3</sub> and water residues. Considering SO<sub>2</sub> as the solvent, the molarity of LiAlCl<sub>4</sub> was 5.2 M.

### 2.4 CuO cathode fabrication with PAN

The as-prepared MYS-CuO (active material) and KB (conducting material) were first mixed at a weight ratio of 6:2 in a mortar with a pestle. The PAN/NMP solution was then added to the mixture and homogenized using a planetary mixer (AR-100, Thinky) at 2000 rpm. The weight ratio of MYS-CuO, KB, and PAN was controlled at 6:2:1. The slurry was cast onto a clean glass plate with a 5 cm doctor blade and annealed in ambient air at 200, 250, and 280 °C for 1 h at a heating rate of 2 °C min<sup>-1</sup> to cyclize the PAN after drying overnight in a vacuum oven at 120 °C. The powder was collected and mixed with PTFE (60 wt% emulsion) using a mortar and pestle to form a clay-like paste. The final composition of the CuO: KB: PAN: PTFE was 6:2:1:1. The thickness of the clay-like paste was controlled to approximately 100 μm using a press-gap-adjustable roller press, and punched into Φ6 discs. The loading mass of the electrode was 10–11 mg cm<sup>-2</sup> with a density of approximately 1 g cc<sup>-1</sup>. The electrodes were dried in a vacuum oven at 120 °C for more than 12 h prior to coin cell fabrication.

### 2.5 Electrochemical measurements

A CR2032 coin-type cell was assembled in a dry room (dew point < -58 °C) using CuO as the working electrode, a 150 μm-thick Li metal sheet as the counter electrode, 200 μL LiAlCl<sub>4</sub>·3SO<sub>2</sub> as the electrolyte, and a 190 μm-thick glass microfiber membrane as the separator. Electrochemical tests were performed using Neware (BTS-4008-5V10mA) and Toyo (TOSCAT-3100) battery testing systems at room temperature (25 °C). The cells were operated galvanostatically at 62.5 mA g<sub>CuO</sub><sup>-1</sup> within the voltage range of 3.2–3.65 V vs. Li/Li<sup>+</sup>. In this study, the capacity and voltage were calculated based on the mass of the CuO cathode material. For the rate capability test, the charge and discharge rates were varied from 0.1 to 1 C (1 C = 300 mA g<sup>-1</sup>). Electrochemical impedance spectroscopy (EIS) measurements were performed using a biologic VSP-100 in the frequency range of 1 MHz to 10 mHz with a voltage perturbation of 5 mV. The electrodes were immersed in the electrolyte for 1 week to activate CuO to CuCl<sub>2</sub>, and then assembled symmetrically in coin cells for EIS measurement.

### 2.6 Characterization

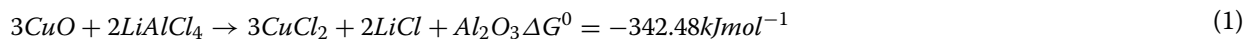
FE-SEM with energy-dispersive X-ray analysis (S-4700, HITACHI) and high-resolution TEM (JEM-2100 F, JEOL) were used to examine the morphology, microstructure, and composition of the as-prepared CuO and its electrodes. For ex situ FESEM observation of CuO electrodes after resting or cycling, the electrode was carefully removed from the coin cell and rinsed with SOCl<sub>2</sub> in an Ar-gas-filled glove box (<1 ppm H<sub>2</sub>O and O<sub>2</sub>) to remove the electrolyte residue. For the ex-situ XRD (D8 DISCOVER, Bruker) measurements, the CuO electrodes were vacuum packed in a polythene sealing bag to prevent phase transformation in the atmosphere because LiCl, CuCl<sub>2</sub>, and CuCl, as electrode resting and cycling products, are sensitive to moisture and air. The surface chemistry of the CuO electrodes after resting was examined using XPS (Thermo Fisher Scientific Co. Inc.). All the XPS spectra were shifted by the same values based on the C 1s peak at 284.8 eV.

## 3 Results and discussion

### 3.1 Limitations of CuO cathode

The separation of the active materials in SO<sub>2</sub>-in-salt systems with self-activating Cu-based cathodes, which can occur during the self-activation reaction and cycling, is attributed to the significant changes in their microstructure, leading to capacity fading [11]. The conversion of the inactive CuO phase into the active CuCl<sub>2</sub> phase via spontaneous chlorination is thermodynamically favorable.

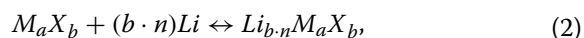
The chlorination reaction of CuO in SO<sub>2</sub>-in-salt electrolytes can be expressed as follows:



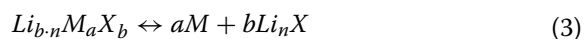
where  $\Delta G^0$  is the calculated Gibbs free energy change for the chlorination reaction.

As described in Additional file 1, CuO spontaneously reacts with LiAlCl<sub>4</sub> in the electrolyte to form thermodynamically stable CuCl<sub>2</sub>, LiCl, and Al<sub>2</sub>O<sub>3</sub>. Moreover, CuO with a monoclinic distorted tetragonal PtS structure transforms into CuCl<sub>2</sub> with a CdI<sub>2</sub>-like layered structure via an anion exchange reaction (Additional file 1: Fig. S1) [26]. The change in the crystal structure and volume expansion during the anion exchange reaction can cause unavoidable morphological changes and separation of the active materials [11].

Moreover, separation of the active materials occurs during the conversion reactions associated with the charge-discharge process. Typically, when the active materials are optimized using nanostructuring strategies, it is expected that their original morphology will be maintained even if their crystal structure changes. Most conversion-type active materials (M<sub>a</sub>X<sub>b</sub>; M = transition metal, such as Mn, Fe, Co, Ni, and Cu; X = anion, such as O, S, Se, F, N, and P) store Li<sup>+</sup> ions via two-step reactions [27, 28]. During the first lithiation step, Li<sup>+</sup> ions are inserted into the crystal lattice of the active material to form intermediate ternary Li–M–X phases as follows:



where  $n$  is the formal oxidation state of  $x$ . During the second lithiation step, as the reaction proceeds gradually, a transition metal precipitates and lithium compounds are formed, as follows:



Owing to the formation of the Li–M–X intermediate phase, the shapes of the M<sub>a</sub>X<sub>b</sub> active material and the transition metal did not change significantly. In contrast, CuCl<sub>2</sub> with a monoclinic structure reacts with Li in the SO<sub>2</sub>-in-salt electrolyte system to form CuCl with a zinc-blende structure and LiCl with a cubic structure, as follows: [9–11]



The ionic radii of anions are larger than those of cations; hence, they play a critical role in determining the shape of the crystal lattice. Therefore, when Cl<sup>−</sup> ions deviate from the original crystal lattice and form

a new phase, the remaining atoms form a new crystal structure. Consequently, the morphology of the active materials changes continuously during the redox reac-

tion between CuCl<sub>2</sub> and CuCl, which occurs during cycling and is accompanied by separation of the active materials.

### 3.2 Effect and modification of carbon materials and CuO

As indicated in Additional file 1: Fig. S2c–f, KB, the 0-D conductive additive promotes the fast conversion of the evenly distributed nanosized CuO particles into CuCl<sub>2</sub>. However, the resulting rapid change in shape led to the separation of the active material and block the conductive path because insulating CuCl<sub>2</sub> covered the conductive KB nanoparticles. In this study, we used CuO microspheres as the active material instead of uniformly distributed CuO nanoparticles. Field-emission scanning electron microscopy (FE-SEM) image of the as-prepared MYS-CuO microspheres is presented in Fig. 1a and Additional file 1: Fig. S4. The MYS-CuO microspheres exhibited a non-porous outer shell structure at ~1 μm in diameter and a partially hollow internal structure comprising nanoparticle clusters (~50 nm in size) inside the cavities. The conversion of CuO into CuCl<sub>2</sub>, which was accelerated by KB, progressed inward from the outside of the MYS-CuO clusters. Therefore, the effect of conductive KB on the conversion reaction was negligible, even though KB and CuO nanoparticles were homogeneously mixed.

The carbon-based conductive agent surrounding the active material played a catalyst-like role, accelerating the self-activation reaction. The FE-SEM images of the carbon-free and several carbon-containing CuO cathodes after immersion in LiAlCl<sub>4</sub>·3SO<sub>2</sub> are presented in Fig. 1b, c, g, and S2c–h. After immersion for 48 h, short CuCl<sub>2</sub> needles grew on the surface of the spherical CuO particles of the carbon-free cathode (Fig. 1b and S2c), and the chemical composition of the needles was confirmed using X-ray diffraction (XRD) (Additional file 1: Fig. S3). Moreover, as the spherical CuO nanoparticles were consumed, wire-shaped CuCl<sub>2</sub> particles were formed at the KB-containing cathode (Fig. 1c, Additional file 1: Fig. S2e, and S3). Owing to its high surface area, 0-D KB provided abundant active sites. Furthermore, KB served as the catalyst and template for the recrystallization of CuCl<sub>2</sub> nanowires with low surface energy [29]. This reaction was similar to the vapor-liquid-solid growth of 1-D structures, thus facilitating the self-activation of the cathode material. However, such changes in the morphology of the active cathode material electrically isolated it from the conductive agent, leading to the deterioration of the



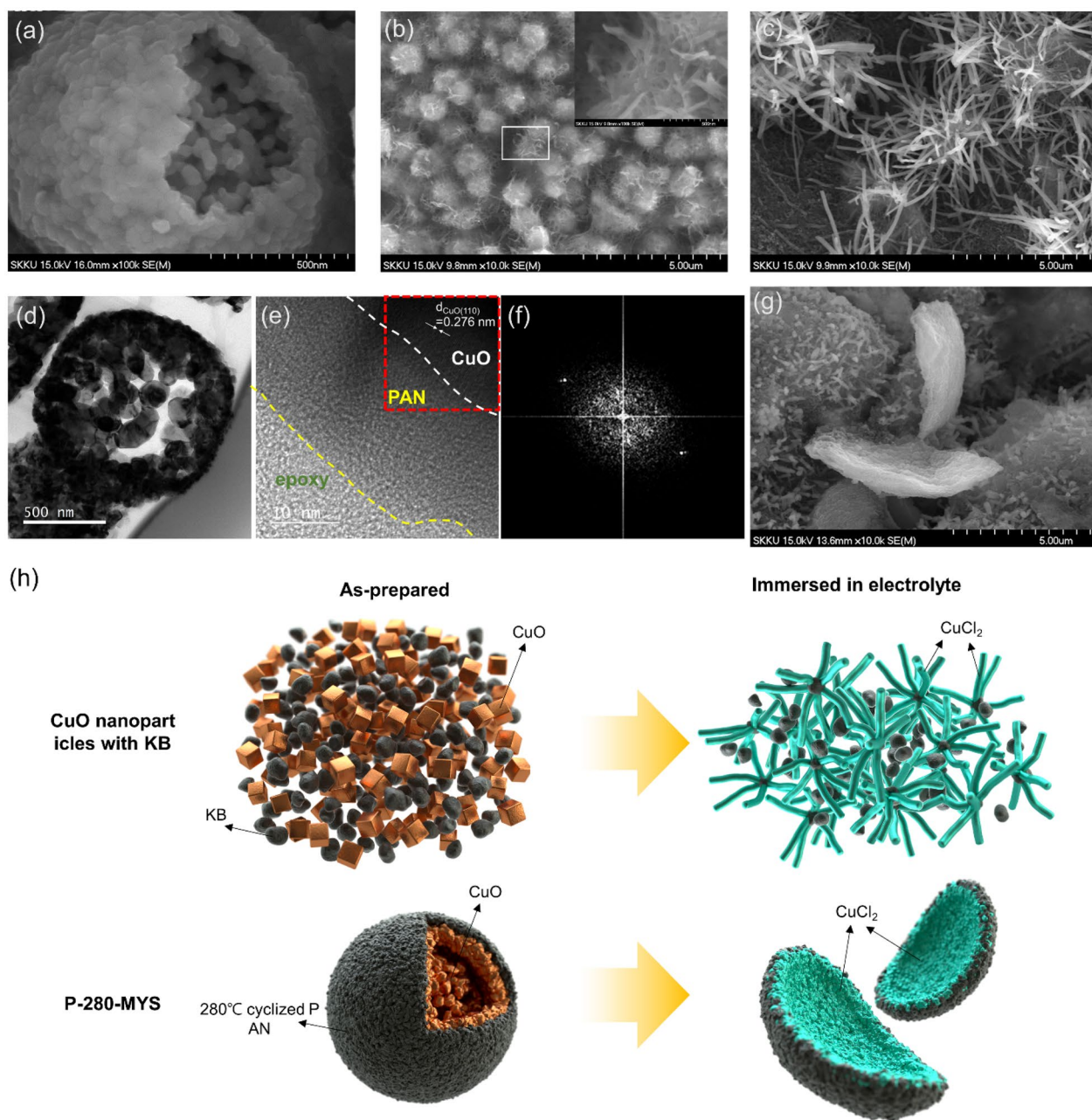


**Fig. 1** Field-emission scanning electron microscopy images of the **a** as-prepared multi-yolk-shell CuO (MYS-CuO) microspheres, **b** carbon-free MYS-CuO cathode (CuO: polytetrafluoroethylene (PTFE) = 6:2), and **c** Ketjen black (KB)-containing MYS-CuO cathode (CuO: KB: PTFE = 6:2:2) after immersion in the electrolyte. **d** Transmission electron microscopy (TEM), and **e** high-resolution TEM images of polyacrylonitrile (PAN)-coated MYS-CuO microspheres cyclized at 280 °C. **f** Fast Fourier transform pattern of the area enclosed by the red dashed square in **e**. **g** KB-and-PAN-containing MYS-CuO cathode cyclized at 280 °C (CuO: KB: PAN: PTFE = 6:2:1:1) after immersion in the electrolyte. **h** Schematic of the structural transformation of the active cathode materials: without carbon coating (top row), with carbon coating (bottom row), before immersion in the electrolyte (left column), and after immersion in the electrolyte (right column). The black and tan squares represent KB particles and MYS-CuO microspheres, respectively

electrochemical properties of the cathode. In addition, the large volume changes during repeated charging–discharging reduced the physical contact between the cathode components, and consequently, the cathode cracks.

To mitigate this volume change, we mixed a solution of PAN in N-methyl-2-pyrrolidone with MYS-CuO and KB to ensure robust conduction pathways. The mixture was subjected to cyclization at 280 °C under ambient air

conditions. The cross-sectional microstructure of the PAN-coated MYS-CuO cyclized at 280 °C (P-280-MYS) was analyzed using focused ion beam microscopy and transmission electron microscopy, respectively, and the results are presented in Fig. 1d and e, respectively. The (100) plane of monoclinic CuO can be observed in the fast Fourier transform pattern of the region enclosed by the dashed red square in Fig. 1e that is illustrated in Fig. 1f. The FE-SEM images and XRD profile of the P-280-MYS cathode after immersion in the electrolyte (Fig. 1g and Additional file 1: Fig. S2g and Fig. S3, respectively) revealed the presence of mossy-like and sprout-shaped  $\text{CuCl}_2$  particles, indicating that cyclized PAN, which is a carbon material containing N-doped delocalized  $\text{sp}^2$   $\pi$ -bonds, affected the formation of the  $\text{CuCl}_2$  phase via the conversion reaction at the cathode. A schematic of the structural transformation of carbon-containing CuO particles and MYS-CuO cathodes during immersion in the electrolyte is depicted in Fig. 1h.

Similar changes in morphology were observed for cathodes comprising hollow CuO nanocubes (CuO HNCs) as the active material with similar cathode compositions. (Additional file 1: Fig. S2 b, d, f, and h) However, the  $\text{CuCl}_2$  particles of the cyclized PAN-containing CuO HNC cathode were plate-shaped (Additional file 1: Fig. S2h) unlike the sprout-shaped  $\text{CuCl}_2$  particles of the P-280-MYS cathode, which was attributed to the initial shape of the CuO nanoparticles.

### 3.3 Characterization of oxidative cyclized PAN

The oxidative cyclization of PAN via heat treatment at 200–300 °C under ambient air converted the polymer into pyrogenic carbon. During this process, the nitrile ( $\text{C}\equiv\text{N}$ ) groups of the PAN chains were converted into  $\text{C}=\text{N}$  and  $\text{C}-\text{N}$  bonds, resulting in a cross-linking ring structure with pyridinic, pyrrolic, and quaternary N atoms. The extent of cyclization depended on the reaction temperature.

To analyze the relationship between the chemical structure and cyclization temperature of the PAN-containing MYS-CuO cathodes, we performed X-ray photoelectron spectroscopy (XPS) and Fourier-transform infrared (FTIR) spectroscopy experiments. The N 1s XPS profiles of the MYS-CuO cathodes with non-cyclized PAN (P-MYS) and PAN cyclized at 280 supplementary Infor°C (P-280-MYS) are illustrated in Fig. 2a–c and Additional file 1: Fig. S5. The only peak at 400.0 eV in the N 1s XPS profile of the P-MYS cathode was attributed to the presence of  $\text{C}\equiv\text{N}$  groups. After cyclization, this peak was broadened by the evolution of three new peaks at 399.2, 400.6, and 401.6 eV, which were ascribed to pyridinic-, pyrrolic-, and quaternary-N, respectively. The

intensities of these peaks increased with increasing cyclization temperature, whereas the intensity of the peak corresponding to the  $\text{C}\equiv\text{N}$  groups decreased (Fig. 2b and Additional file 1: Fig. S5). The structures of  $\text{C}\equiv\text{N}$  and pyridinic-, pyrrolic-, and quaternary-N groups are shown in Fig. 2c. The peaks in the N 1s XPS profile were upshifted by 0.5 eV compared with the values reported in the literature [30, 31]. The shift was attributed to the strong interaction between the N species and Cu(II) sites of CuO [32–34].

The FTIR spectra of the raw and cyclized PAN powders at temperatures between 150 and 300 °C are presented in Fig. 2d. As the oxidative cyclization temperature increased, the intensities of the peaks at 2241  $\text{cm}^{-1}$  ( $\text{C}\equiv\text{N}$  group), 2935, and 2870  $\text{cm}^{-1}$  ( $\text{C}-\text{H}$  stretching of the  $-\text{CH}_2-$  groups of the PAN backbone), 1450  $\text{cm}^{-1}$  ( $\text{C}-\text{H}$  bending vibrations of the  $-\text{CH}_2-$  groups of the PAN backbone), and 1358  $\text{cm}^{-1}$  ( $\text{C}-\text{H}$  bending vibrations of the  $-\text{CH}_2-$  and  $-\text{CH}-$  groups of the PAN backbone) decreased. Three new bands at 1580  $\text{cm}^{-1}$  (attributed to the stretching of the  $\text{C}=\text{C}$  bonds, cyclic  $\text{C}=\text{N}$  bonds, and in-plane bending of the  $\text{N}-\text{H}$  bonds), 1380  $\text{cm}^{-1}$  (assigned to the bending vibration of the  $\text{C}-\text{H}$  and  $\text{N}-\text{H}$  bonds in the rings), and 810  $\text{cm}^{-1}$  (ascribed to the  $\text{C}=\text{CH}$  bonds of the aromatic rings) emerged at 200 °C. The intensities of these bands increased with increasing cyclization temperature, revealing that the  $\text{C}\equiv\text{N}$  groups were converted into a cyclic structure when the temperature exceeded 200 °C. The extent of reaction (EOR) for the cyclization of PAN with respect to the heat treatment temperature (Fig. 2e) was calculated as follows:

$$\text{EOR}(\%) = \frac{I_{1580}}{(I_{1580} + I_{2241})} \times 100 \quad (5)$$

where  $I_{1580}$  and  $I_{2241}$  are the intensities of the bands at 1580 and 2241  $\text{cm}^{-1}$ , respectively. The EOR was approximately 100% at temperatures higher than 280 °C. The differential scanning calorimetry profile of PAN revealed that it underwent pyrolysis, and exothermic peaks were observed at temperatures higher than 300 °C (Additional file 1: Fig. S6).

The presence of O during the oxidative cyclization reaction led to the formation of numerous O-containing groups. (Fig. 2d) In particular, bands at 1720  $\text{cm}^{-1}$  (ascribed to the stretching of the  $\text{C}=\text{O}$  bonds in ketones, aldehydes, and  $-\text{COOH}$  groups), 1662  $\text{cm}^{-1}$  (attributed to the stretching of the  $\text{C}=\text{O}$  bonds in the highly conjugated acridone rings), 1161–1200  $\text{cm}^{-1}$  (corresponding to the stretching of the  $\text{C}-\text{O}$  bonds), and 1250  $\text{cm}^{-1}$  (attributed to the asymmetric stretching of the  $\text{C}-\text{O}-\text{C}$  bonds) were observed in the FTIR spectra of the PAN-containing MYS-CuO cathodes cyclized at temperatures higher than 200 °C.

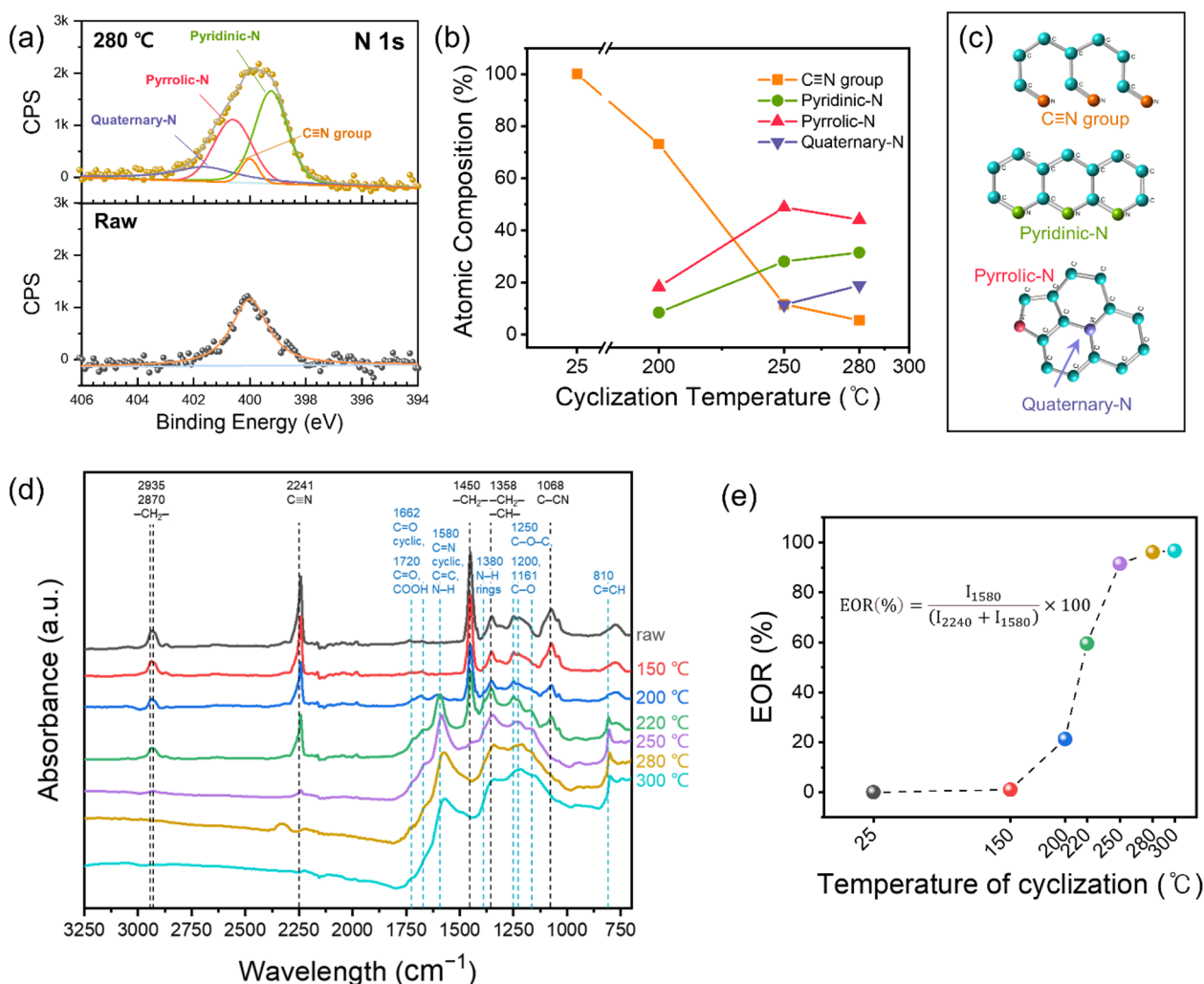


**Fig. 2** Characterization of PAN-containing CuO cathodes and PAN powder before and after cyclization at several temperatures. **a** N 1s X-ray photoelectron spectroscopy (XPS) profiles of CuO cathodes with non-cyclized PAN and 280 °C cyclized PAN, marked with “Raw” and “280 °C”, respectively. **b** Atomic composition of N-containing functional groups at different cyclization temperatures according to their N 1s XPS profiles. **c** Structures of C≡N and pyridinic-, pyrrolic-, and quaternary-N groups. **d** Fourier-transform infrared (FTIR) spectra of the raw and cyclized PAN powder at temperatures in the range of 150–300 °C. **e** Extent of ratio (EOR) of the PAN cyclization reaction calculated using FTIR data

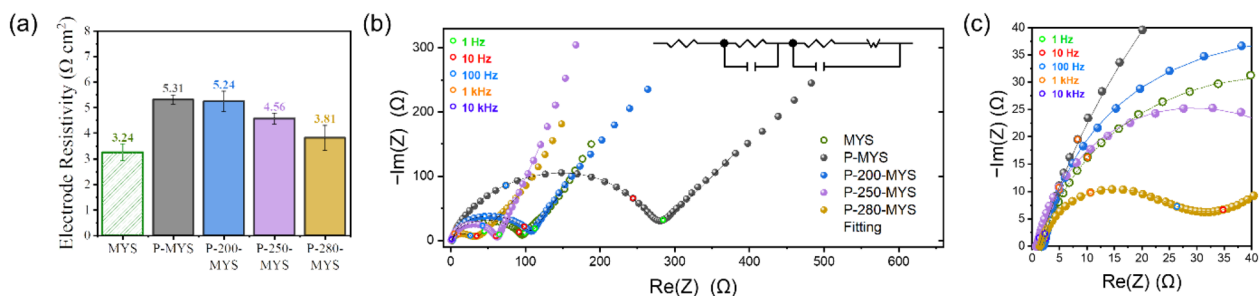


**Fig. 3** **a** Resistivity of the as-prepared multi-yolk-shell (MYS)-CuO cathodes with non-cyclized PAN (P-MYS; CuO: KB: PAN: PTFE = 6:2:1:1), with PAN cyclized at 200, 250, and 280 °C (P-200-MYS, P-250-MYS, and P-280-MYS, respectively; CuO: KB: PAN: PTFE = 6:2:1:1), and without PAN (MYS, CuO: KB: PTFE = 6:2:2). **b** Nyquist plots of the symmetric cells featuring different cathodes after resting for 1 week. **c** High-frequency region of the Nyquist plots in **b**



### 3.4 Characterization of PAN-coated MYS-CuO cathodes

The N-doping of carbon materials could increase their electron transport rate, electron shuttling efficiency, and electron carrier concentration. The resistance of the P-280-MYS cathode was as low as that of the KB-containing MYS-CuO cathode (CuO: KB: PTFE = 6:2:2). The resistivity of the cathode containing non-cyclized PAN (P-MYS, CuO: KB: PAN: PTFE = 6:2:1:1) was high ( $5.31 \Omega \text{ cm}^2$ ; Fig. 3a). As the cyclization temperature was increased from 200 °C (P-200-MYS) to 250 °C (P-250-MYS), and 280 °C (P-280-MYS), the cathode resistivity decreased to 5.24, 4.56, and  $3.81 \Omega \text{ cm}^2$ , respectively (Fig. 3a). These results demonstrated that the formation of N-doped carbon with delocalized  $\text{sp}^2$   $\pi$ -bonds during PAN cyclization improved the electrical conductivity of the cathode.

To evaluate the charge transfer capability of the cathodes after resting, we performed electrochemical impedance spectroscopy measurements for symmetric cells featuring cathodes cyclized at different temperatures after resting for a week. The impedance of the P-280-MYS cathode after self-activation was the lowest, indicating that the N-doped carbon surrounding the active materials lowered the charge-transfer resistance ( $R_{ct}$ ) of the cathode (Fig. 3b and c). Moreover, the N-doped carbon particles captured Cu ions, preventing their migration outside the carbon coating, and acted as active sites for the recrystallization of  $\text{CuCl}_2$  and  $\text{CuCl}$  during charging-discharging.

### 3.5 Electrochemical performance

The electrochemical performances of the MYS, P-MYS, P-200-MYS, P-250-MYS, and P-280-MYS cathodes for Li metal dual-ion batteries with  $\text{SO}_2$ -in-salt electrolytes are presented in Fig. 4. The discharge capacity and capacity retention of the batteries significantly depended on the cathode resistivity and  $R_{ct}$ . The initial discharge specific capacity of the P-280-MYS cathode was the highest ( $315.9 \text{ mAh g}^{-1}$ ) among all analyzed cathodes. This value was comparable to the theoretical capacity of  $336.9 \text{ mAh g}^{-1}$  at 0.2 C, which corresponded to an energy density of  $\sim 1295 \text{ Wh kg}_{\text{CuO}}^{-1}$ . Moreover, the P-280-MYS cathode exhibited excellent cycling stability, with a capacity retention of  $\sim 84\%$  ( $\sim 266.8 \text{ mAh g}^{-1}$ ) after 200 cycles. The discharge specific capacity of the MYS cathode faded faster than that of the P-280-MYS cathode, dropping from  $284.2 \text{ mAh g}^{-1}$  in the 1st cycle to  $177.0 \text{ mAh g}^{-1}$  in the 200th cycle, with a capacity retention rate of only 62.3%. The P-200-MYS and P-250-MYS cathodes exhibited good capacity retention in the 200th cycle, compared to their highest capacities of 87.9% and 83.6%, respectively (the highest specific capacity was  $160.2 \text{ mAh g}^{-1}$  in the 124th cycle for P-200-MYS and  $235.7 \text{ mAh g}^{-1}$

in the first cycle for P-250-MYS). We speculated that the O-containing groups formed by heat treatment in an oxygenated environment (found in the FT-IR analysis, as shown in Fig. 2d) may be responsible for the improved cycle retention of P-200-MYS, P-250-MYS, and P-280-MYS cathodes, as PAN functionalized with negatively charged groups was reported to be an adsorbent for metal ions that can suppress the separation of Cu ions from the cathode [35–37]. Meanwhile, the O-containing groups and residual  $\text{C}\equiv\text{N}$  groups of P-200-MYS and P-250-MYS limited their electrical conductivity, which contributed to the large initial  $\Delta V$  values of the cathodes, as illustrated in their voltage profiles (Fig. 4b). This effect was overcome as the cycles progressed (Fig. 4c). The  $\Delta V$  values were calculated at a depth of discharge (DOD) of 50% and a state of charge (SOC) of 50%. In addition,  $\text{C}\equiv\text{N}$  groups with delocalized electron structures, typically repel anions and attract cations, thereby hindering ion transport during charging-discharging. This could be the reason why the  $\Delta V$  values of P-MYS increased after cycling. (Figs. 2a and 4c)

The charge-discharge profiles of the MYS-CuO cathode during the 1st and 233rd cycles are presented in Fig. 4b and c, respectively. The cell voltage during discharging ( $V_{dis}$ ) and charging ( $V_{ch}$ ) is expressed as follows:

$$V_{dis} = V_{emf} - Ir \quad (6)$$

and

$$V_{ch} = V_{emf} + Ir \quad (7)$$

where  $V_{emf}$  is the electromotive force of the battery,  $I$  is the current, and  $r$  is the internal resistance of the cell, which includes contact resistance, electrolyte resistance, activation polarization, and concentration polarization of the cathode.

The fluctuations in the  $\Delta V$  value suggested that the  $r$  value changed during cycling. During heat treatment, the  $\text{C}\equiv\text{N}$  groups of PAN were converted into amide groups owing to cyclization or the so-called “stabilization” process. Cyclized PAN is an N-doped carbon material, and its electrical conductivity is higher than that of the raw PAN (P-MYS). Furthermore, the N-doped carbon with delocalized  $\text{sp}^2$   $\pi$ -bonds during cyclization improves the adhesion to the active material [38, 39], leading to faster ion transfer and compatible mechanical resiliency. Because all the  $\text{C}\equiv\text{N}$  groups of PAN heat-treated at 280 °C were converted into amide groups, P-MYS-280 was the only cathode that retained a high discharge capacity over 200 cycles, and its  $\Delta V$  value was constant, as presented in Fig. 4d.

The rate capabilities of the cathodes are shown in Fig. 4e. The charge and discharge rate capabilities were



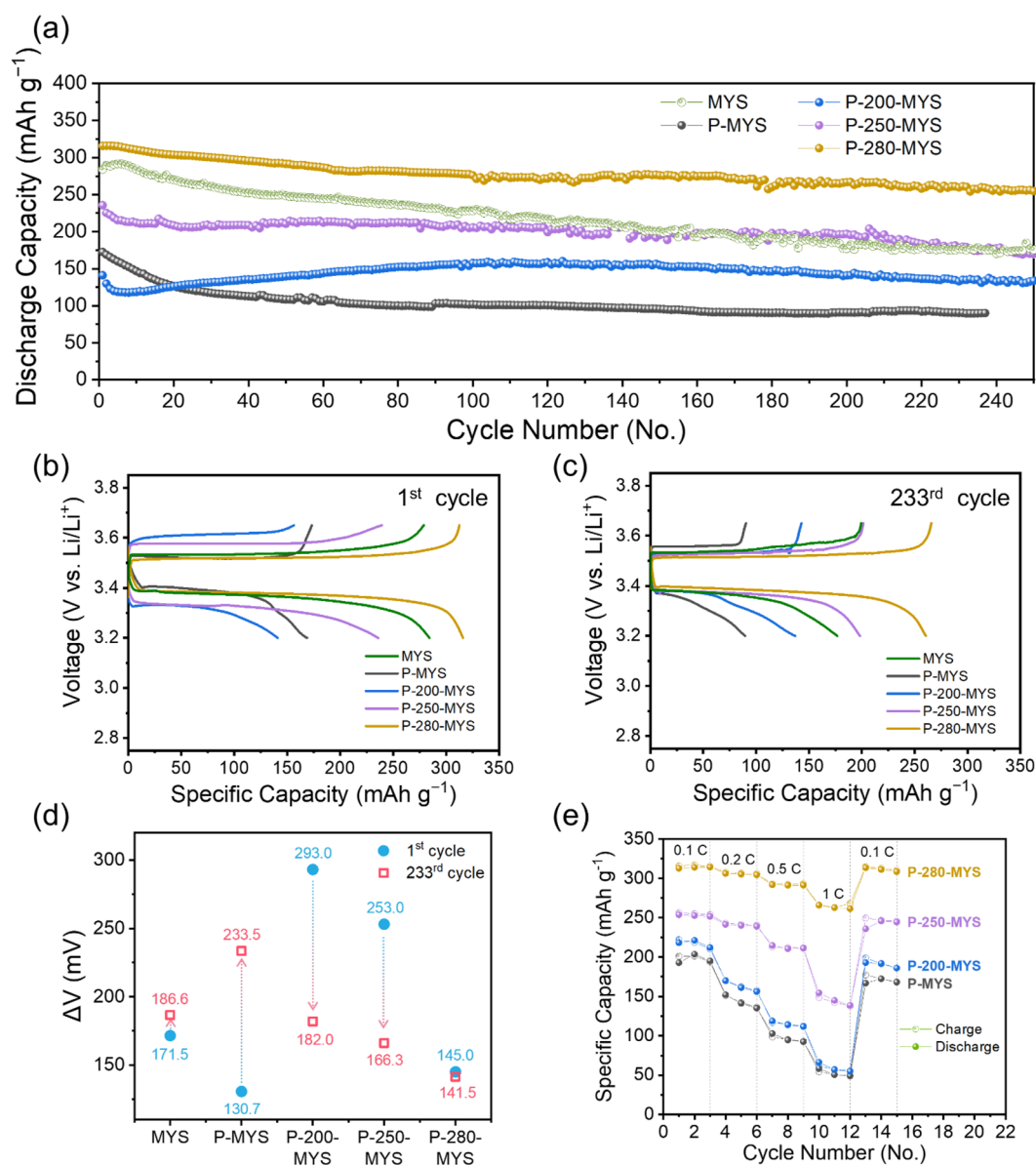


**Fig. 4** Electrochemical performance of cathodes. **a** Cyclic performance. Galvanostatic voltage profiles at the **b** 1st and **c** 233rd cycles of the multi-yolk-shell (MYS)-CuO cathodes without PAN (MYS), with non-cyclized PAN (P-MYS), and with PAN cyclized at 200, 250, and 280 °C (P-200-MYS, P-250-MYS, and P-280-MYS, respectively) at 0.2 C. **d** Potential differences calculated at a depth of discharge of 50% and state of charge of 50% using the galvanostatic voltage profiles in **b** and **c**. **e** Rate capability of the cathodes at 0.1, 0.2, 0.5, and 1 C (1 C = 300 mA g<sup>-1</sup> for CuO).

measured at several current rates between 0.1 and 1 C and in the voltage range of 3.2–3.7 V vs. Li<sup>+</sup>/Li. The charge and discharge rates were maintained constant. The capacity of P-280-MYS was the highest at all C-rates and remained above 250 mAh g<sup>-1</sup> even at a high rate of 1 C, whereas the other cathodes exhibited relatively poor rate properties.

In the Ragone plot shown in Fig. 5, the rate performance of the MYS-CuO cathode (P-MYS-280) is compared with that of state-of-the-art cathode materials for

Li/Na-SO<sub>2</sub> batteries. The simple nanosizing improved the energy density as a result of the Li-Cu<sub>2</sub>O nanocrystals [9] and Li-CuO hollow nanocubes (HNCs) [11] shown in Fig. 5; however, as discussed earlier, the improvements in the power density are limited. The energy density of MYS-CuO, which is a nanocluster, was over 900 Wh kg<sup>-1</sup> at any given power density. Moreover, the C-rate was maintained at 1 C during charging, and there was no significant deterioration in the discharge capacity (the

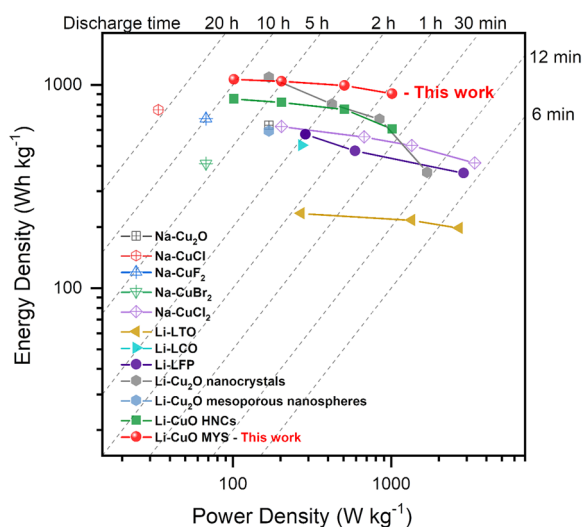


**Fig. 5** Ragone plot for comparison of the energy density and power density among state-of-the-art cathodes of Li/Na-SO<sub>2</sub> battery with optimized rate performance as reported in the literatures.[6, 7, 9–11, 40, 41]

energy density and power density at 1 C were 903 Wh kg<sup>-1</sup> and 1020 W kg<sup>-1</sup>, respectively).

### 3.6 Morphology evolution of PAN-coated MYS-CuO during charge-discharge

Changes in the microstructure of the P-280-MYS cathode during charging and discharging were evaluated using FE-SEM to elucidate the reasons for its excellent electrochemical performance. The P-280-MYS cathodes were disassembled at DODs and SOC of 25%, 50%, and 100% of the first cycle (Fig. 6a), and their corresponding FE-SEM images are presented in Fig. 6b–g and Additional file 1: Fig. S7a. During the early discharge stage (DOD of 25%), the buds that sprouted from the seeds (MYS) were planted in the field (cathode) and convexly protruded on the cathode surface. Thereafter, the buds gradually swelled and opened as the DOD increased to 50% and turned into blooming flowers when the cathode was completely discharged at a DOD of 100% (Fig. 6b–d and Additional file 1: Fig. S7a). The XRD patterns and energy-dispersive X-ray spectroscopy mappings of the cathodes revealed that the petals produced during discharging consisted of CuCl and LiCl (Additional file 1: Fig. S8). During charging, the CuCl and LiCl petals at the center of the flower gradually disappeared (Fig. 6e and f). Finally, the active material returned to its initial shape at 100% SOC (Fig. 6g and Additional file 1: Fig. S7a). The

overall morphology evolution of the active material particles during the first charge–discharge cycle is illustrated in Fig. 6h. The MYS-CuO microspheres surrounded by cyclized PAN were converted to CuCl<sub>2</sub> through a self-activation process. At this point, recrystallization caused a significant change in the volume of the initial yolk–shell microspheres, which split and resemble germinating seeds. Upon discharge, the Cl<sup>-</sup> ions originating from CuCl<sub>2</sub> combined with the Li<sup>+</sup> ions in the electrolyte to form LiCl, and the reduced monovalent Cu<sup>+</sup> ions recrystallized with the residual Cl<sup>-</sup> ions to form CuCl. The initial CuCl<sub>2</sub> particles presented curved shapes, with the convex part covered by the cyclized PAN and the concave part in direct contact with the electrolyte. As a result, Cl<sup>-</sup> ions easily diffused into the concave parts of the CuCl<sub>2</sub> particles, and the byproducts generated via discharge grew inward and exhibited a bud-like morphology. When the generated discharge products grew larger than the space inside the buds, the discharge product particles bloomed outward to form a flower-like morphology. During charging, the byproducts disappeared from the center of the flower shape and returned to the sprout shape, similar to the process described above. It is possible to provide a variable space inside the concave area of the active material and ensure constant conductive pathways through the convex side.

## 4 Conclusion

The separation of active cathode materials during the ion-exchange and recrystallization reactions of the self-activation and cyclic conversion steps limited the specific capacity and decreased the cycle retention. We demonstrated that the 1 μm MYS-CuO microspheres served as an excellent active cathode material. Such morphological design ensured a fast CuO self-activation reaction to CuCl<sub>2</sub> and prevented the conductivity of the KB conductive material from decreasing owing to the dispersed and rapid reactions. Oxidative cyclized PAN containing N-doped delocalized sp<sup>2</sup> π-bonds was used as the recrystallization catalyst/template for the cathode because of the effect of conductive carbon on the self-activation and cyclic conversion of the active cathode materials. The P-280-MYS cathode exhibited an initial specific capacity of 315.9 mAh g<sup>-1</sup> (93.8% of the theoretical value) at 0.2 C, an energy density of 1295.19 Wh kg<sup>-1</sup>, and a retention rate of 84.46% after 200 cycles. The flower-blooming-like cathode morphology observed during the discharging and charging of the P-280-MYS cathode demonstrated that the cyclized PAN served as a

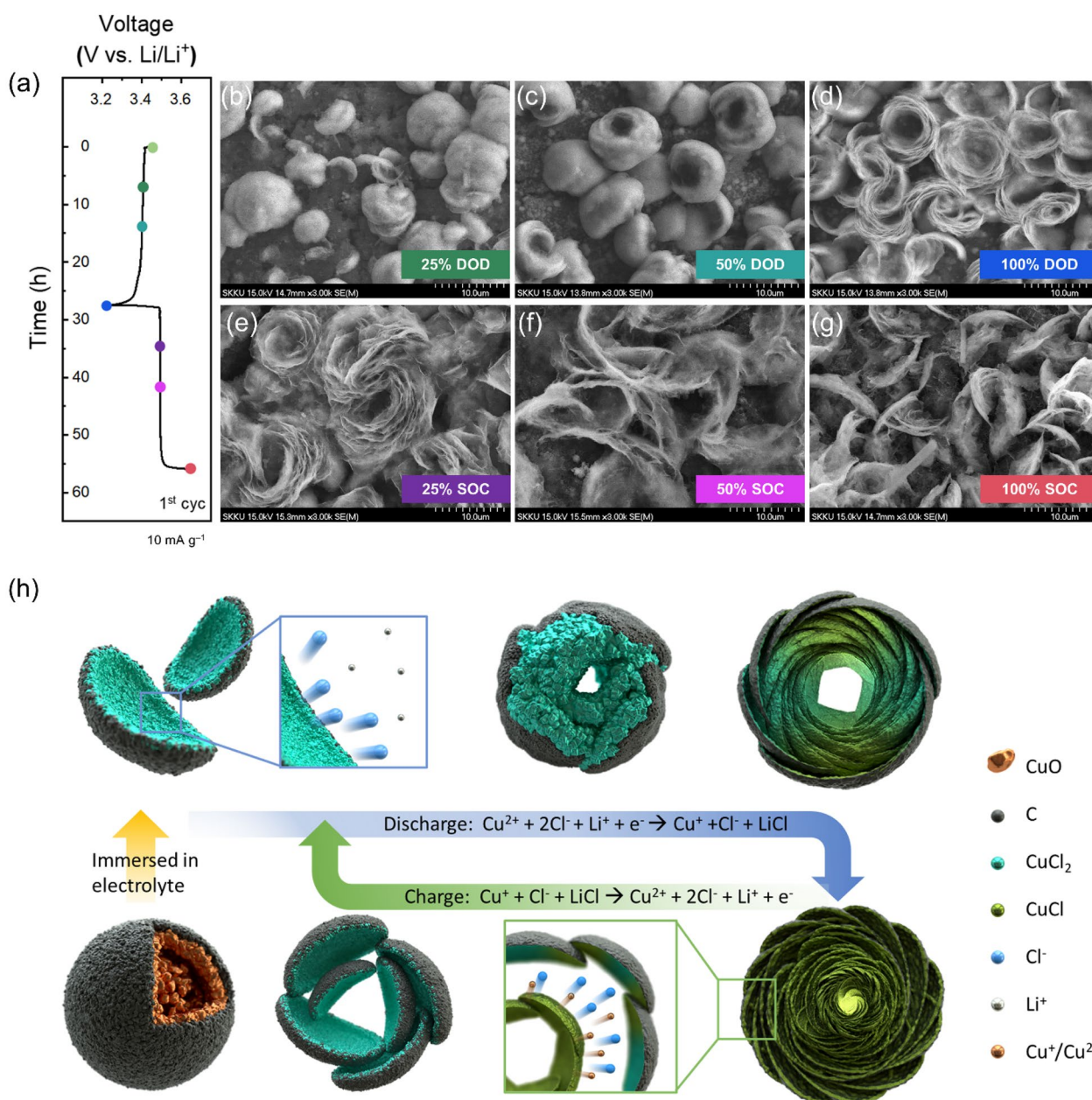


**Fig. 6** Evolution of particle morphology of the PAN-coated MYS-CuO cyclized at 280 °C (P-280-MYS) used as the cathode during charging-discharging. **a** Voltage profile of the P-280-MYS cathode at a current density of 10 mA g<sup>-1</sup> during the first charge-discharge cycle. Surface morphology of the P-280-MYS cathode at depths of discharge (DODs) of **b** 25%, **c** 50%, and **d** 100% and states of charge (SOCs) of **e** 25%, **f** 50%, and **g** 100%. **h** Schematic of the overall morphological evolution of the active material of the P-280-MYS cathode during the first charge-discharge cycle

template for recrystallization of the active material, minimizing its separation and improving the electrochemical performance of the cathode. Our results promote the use of non-flammable Li metal dual-ion battery systems with excellent specific capacities and cycle retention performances. Moreover, our study provides constructive perspectives for the optimization of conversion cathodes

through reactions that involve significant morphological changes.

### Supplementary Information

The online version contains supplementary material available at <https://doi.org/10.1186/s40580-022-00353-3>.



**Additional file 1: Figure S1.** Schematic of conversion reaction for the cathode active materials during resting and cycling. Crystal structure and parameters of CuO, CuCl, and CuCl<sub>2</sub> are illustrated. **Figure S2.** FE-SEM images of as-prepared (a) MYS-CuO and (b) CuO hollow nanocubes (HNCs). (c-h) FE-SEM images for electrodes after immersion in electrolyte, including no carbon electrodes with (c) MYS-CuO and (d) CuO HNCs, KB containing electrodes (CuO : KB : PTFE = 6 : 2 : 2) with (e) MYS-CuO (MYS-CuO+KB) and (f) CuO HNCs (CuO HNCs+KB), and cyclized PAN containing electrodes (CuO : KB : PAN : PTFE = 6 : 2 : 1 : 1) with (g) MYS-CuO (MYS-CuO+KB+PAN) and (h) CuO HNCs (CuOHNCs+KB+PAN). **Figure S3.** XRD patterns of as-prepared MYS-CuO, and electrodes with different compositions after immersion in electrolyte. As shown in Figure S2c-f and Figure S3, after immersion in the electrolyte, more, thicker and longer CuCl<sub>2</sub> nanorods or nanowires were observed on CuO cathodes containing 0-D KB compared to carbon-free CuO cathodes, indicating that KB promoted the conversion of CuO to CuCl<sub>2</sub>. In the absence of KB, well-dispersed nano-sized CuO HNCs were converted to needle-like CuCl<sub>2</sub> more rapidly compared to 1-μm MYS-CuO. **Figure S4.** (a-b) SEM images for the broken particles of as-prepared MYS-CuO. (c-d) Low magnification SEM images of as-prepared MYS-CuO. **Figure S5.** N 1s XPS profiles for MYS-CuO electrode with PAN cyclized at different temperatures. **Figure S6.** Differential scanning calorimetry thermograms of PAN powder, PAN-coated MYS-CuO, and bare MYS-CuO (a) before and (b) after heat treatment at 280 °C from 25 to 500 °C with air flowing at a heating rate of 2 °C min<sup>-1</sup>. **Figure S7.** (a) FE-SEM images of bare P-280-MYS electrode and P-280-MYS electrodes after resting and 1st discharge and charge. (b) FE-SEM images of P-280-MYS electrode after 50th discharge. **Figure S8.** (a) XRD patterns for raw, rested, discharged, and charged P-280-MYS electrodes. FE-SEM and EDS mapping images of (b) rested, (c) fully discharged, and (d) fully charged P-280-MYS electrodes.

## Acknowledgements

Not applicable.

## Author contributions

SL performed materials synthesis, characterization and electrochemical measurements and analyzed the data, wrote the original manuscript. JHL and SMH designed the experiments, provided technical feedback, revised the manuscript. YJK supervised the students while developing the manuscript, revising the manuscript and funding acquisition. All authors read and approved the final manuscript.

## Funding

This work was supported by a grant from the Korea Evaluation Institute of Industrial Technology (KEIT) funded by the MOTIE (NO. 20012341) of the Republic of Korea.

## Availability of data and materials

The datasets used and/or analyzed during the current study are available from the corresponding author on reasonable request.

## Declarations

## Competing interests

The authors declare no competing interests.

Received: 24 September 2022 Accepted: 25 December 2022

Published online: 13 January 2023

## References

1. B. Liu, R. Fang, D. Xie, W. Zhang, H. Huang, Y. Xia, X. Wang, X. Xia, J. Tu, Revisiting scientific issues for industrial applications of lithium-sulfur batteries. *Energy Environ Mater* **1**, 196–208 (2018). <https://doi.org/10.1002/eeem.2.12021>

2. J. Lai, Y. Xing, N. Chen, L. Li, F. Wu, R. Chen, Electrolytes for rechargeable lithium-air batteries. *Angew Chem. Int. Ed* **59**, 2974–2997 (2020). <https://doi.org/10.1002/anie.201903459>
3. G. Jeong, H. Kim, J.H. Park, J. Jeon, X. Jin, J. Song, B.-R. Kim, M.-S. Park, J.M. Kim, Kim. Nanotechnology enabled rechargeable Li–SO<sub>2</sub> batteries: another approach towards post-lithium-ion battery systems. *Energy Environ. Sci* **8**(11), 3173–3180 (2015). <https://doi.org/10.1039/C5EE01659B>
4. D. Foster, H. Kuo, C. Schlaikjer, A. Dey, New highly conductive inorganic electrolytes: the liquid solvates of the alkali and alkaline earth metal tetrachloroaluminates. *J. Electrochem. Soc* **135**(11), 2682 (1988). <https://doi.org/10.1149/1.2095410>
5. G. Jeong, H. Kim, H.S. Lee, Y.-K. Han, J.H. Park, J.H. Jeon, J. Song, K. Lee, T. Yim, Kim. A room-temperature sodium rechargeable battery using an SO<sub>2</sub>-based nonflammable inorganic liquid catholyte. *Sci. Rep* **5**, 12827 (2015). <https://doi.org/10.1038/srep12827>
6. T. Gao, B. Wang, L. Wang, G. Liu, F. Wang, H. Luo, D. Wang, LiAlCl<sub>4</sub>·3SO<sub>2</sub> as a high conductive, non-flammable and inorganic non-aqueous liquid electrolyte for lithium ion batteries. *Electrochim. Acta* **286**, 77–85 (2018). <https://doi.org/10.1016/j.electacta.2018.08.033>
7. B.R. Kim, G. Jeong, A. Kim, Y. Kim, M.G. Kim, H. Kim, Kim. High performance Na–CuCl<sub>2</sub> rechargeable battery toward room temperature ZEBRA-type battery. *Adv. Energy Mater* **6**(20), 1600862 (2016). <https://doi.org/10.1002/aenm.201600862>
8. A. Dey, W. Bowden, H. Kuo, M. Gopikanth, C. Schlaikjer, Foster. Inorganic electrolyte Li/CuCl<sub>2</sub> rechargeable cell. *J. Electrochem. Soc* **136**(6), 1618 (1989). <https://doi.org/10.1149/1.2096980>
9. K.-H. Kwak, H.J. Suh, A. Kim, S. Park, J. Song, S. Li, Y. Kim, G. Jeong, H. Kim, Y.-J. Kim, Reversible dual-ion battery via mesoporous Cu<sub>2</sub>O cathode in SO<sub>2</sub>-in-salt non-flammable electrolyte. *Nano Energy* **66**(2019) 104138. <https://doi.org/10.1016/j.nanoen.2019.104138>
10. A. Kim, H. Jung, J. Song, J. Lee, G. Jeong, Y.J. Kim, H. Kim, Self-formulated Na-based dual-ion battery using nonflammable SO<sub>2</sub>-based inorganic liquid electrolyte. *Small* (2019). <https://doi.org/10.1002/smll.201902144>
11. S. Li, J.-H. Lee, S.M. Hwang, J.-B. Yoo, H. Kim, Y.-J. Kim, Natural activation of CuO to CuCl<sub>2</sub> as a cathode material for dual-ion lithium metal batteries. *Energy Storage Mater* **41**, 466–474 (2021). <https://doi.org/10.1016/j.jensm.2021.06.022>
12. S.-H. Yu, X. Feng, N. Zhang, J. Seok, H.D. Abruña, Understanding conversion-type electrodes for lithium rechargeable batteries. *Acc. Chem. Res* **51**(2), 273–281 (2018). <https://doi.org/10.1021/acs.accounts.7b00487>
13. Y. Lu, L. Yu, X.W. Lou, Nanostructured conversion-type anode materials for advanced lithium-ion batteries. *Chem* **4**(5), 972–996 (2018). <https://doi.org/10.1016/j.chempr.2018.01.003>
14. F. Wu, G. Yushin, Conversion cathodes for rechargeable lithium and lithium-ion batteries. *Energy Environ. Sci* **10**(2), 435–459 (2017). <https://doi.org/10.1039/c6ee02326f>
15. K. Zhang, X. Han, Z. Hu, X. Zhang, Z. Tao, J. Chen, Nanostructured mn-based oxides for electrochemical energy storage and conversion. *Chem. Soc. Rev* **44**(3), 699–728 (2015). <https://doi.org/10.1039/C4CS00218K>
16. W. Qi, J.G. Shapter, Q. Wu, T. Yin, G. Gao, D. Cui, Nanostructured anode materials for lithium-ion batteries: principle, recent progress and future perspectives. *J. Mater. Chem. A* **5**(37), 19521–19540 (2017). <https://doi.org/10.1039/C7TA05283A>
17. L. Fei, Y. Xu, X. Wu, Y. Li, P. Xie, S. Deng, S. Smirnov, H. Luo, SBA-15 confined synthesis of TiNb<sub>2</sub>O<sub>7</sub> nanoparticles for lithium-ion batteries. *Nanoscale* **5**(22), 11102–11107 (2013). <https://doi.org/10.1039/C3NR03594H>
18. G. Chen, L. Yan, H. Luo, S. Guo, Nanoscale engineering of heterostructured anode materials for boosting lithium-ion storage. *Adv. Mater* **28**(35), 7580–7602 (2016). <https://doi.org/10.1002/adma.201600164>
19. Z. Wang, D. Luan, S. Madhavi, C.M. Li, Lou. α-Fe<sub>2</sub>O<sub>3</sub> nanotubes with superior lithium storage capability. *Chem. Commun* **47**(28), 8061–8063 (2011). <https://doi.org/10.1039/C1CC12111A>
20. X. Wang, J. Feng, Y. Bai, Q. Zhang, Y. Yin, Synthesis, properties, and applications of hollow micro-/nanostructures. *Chem. Rev* **116**(18), 10983–11060 (2016). <https://doi.org/10.1021/acs.chemrev.5b00731>
21. J. Qi, X. Lai, J. Wang, H. Tang, H. Ren, Y. Yang, Q. Jin, L. Zhang, R. Yu, G. Ma, Multi-shelled hollow micro-/nanostructures. *Chem. Soc. Rev* **44**(19), 6749–6773 (2015). <https://doi.org/10.1039/C5CS00344J>
22. S. Han, B. Jang, T. Kim, S.M. Oh, T. Hyeon, Simple synthesis of hollow tin dioxide microspheres and their application to lithium-ion battery anodes.



- Adv. Funct. Mater **15**(11), 1845–1850 (2005). <https://doi.org/10.1002/adfm.200500243>
23. D. Bresser, S. Passerini, B. Scrosati, Leveraging valuable synergies by combining alloying and conversion for lithium-ion anodes. *Energy Environ. Sci* **9**(11), 3348–3367 (2016). <https://doi.org/10.1039/C6EE02346K>
  24. H.B. Wu, G. Zhang, L. Yu, X.W.D. Lou, One-dimensional metal oxide–carbon hybrid nanostructures for electrochemical energy storage. *Nanoscale Horiz* **1**(1), 27–40 (2016). <https://doi.org/10.1039/C5NH00023H>
  25. P.-Y. Chen, M. Liu, T.M. Valentin, Z. Wang, R. Spitz Steinberg, J. Sodhi, I.Y. Wong, Hurt. Hierarchical metal oxide topographies replicated from highly textured graphene oxide by intercalation templating. *ACS nano* **10**(12), 10869–10879 (2016). <https://doi.org/10.1021/acsnano.6b05179>
  26. A.F. Wells, *Structural inorganic chemistry* (Oxford University Press, Oxford, 2012)
  27. X.Y. Yu, L. Yu, X.W. Lou, Metal sulfide hollow nanostructures for electrochemical energy storage. *Adv. Energy Mater* **6**(3), 1501333 (2016). <https://doi.org/10.1002/aenm.201501333>
  28. J. Cabana, L. Monconduit, D. Larcher, M.R. Palacin, Beyond intercalation-based Li-ion batteries: the state of the art and challenges of electrode materials reacting through conversion reactions. *Adv. Mater* **22**(35), E170–E192 (2010). <https://doi.org/10.1002/adma.201000717>
  29. P. Serp, B. Machado, *Nanostructured Carbon Materials for Catalysis*, Chap. 1. Carbon (Nano)materials for Catalysis (Royal Society of Chemistry, 2015). <https://doi.org/10.1039/9781782622567-00001>
  30. D. Guo, R. Shibuya, C. Akiba, S. Saji, T. Kondo, J. Nakamura, Active sites of nitrogen-doped carbon materials for oxygen reduction reaction clarified using model catalysts. *Science* **351**(6271), 361–365 (2016). <https://doi.org/10.1126/science.aad0832>
  31. Y.R. Park, H.Y. Jeong, Y.S. Seo, W.K. Choi, Y.J. Hong, Quantum-dot light-emitting diodes with nitrogen-doped carbon nanodot hole transport and electronic energy transfer layer. *Sci. Rep* **7**(1), 1–13 (2017). <https://doi.org/10.1038/srep46422>
  32. X. Li, L. Qin, Y. Zhang, Z. Xu, L. Tian, X. Guo, G. Zhang, Self-assembly of mn (II)-amidoximated PAN polymeric beads complex as reusable catalysts for efficient and stable heterogeneous electro-fenton oxidation. *ACS Appl. Mater. Interfaces* **11**(4), 3925–3936 (2019). <https://doi.org/10.1021/acsami.8b18704>
  33. Q. Luo, X. Yang, X. Zhao, D. Wang, R. Yin, X. Li, J. An, Facile preparation of well-dispersed ZnO/cyclized polyacrylonitrile nanocomposites with highly enhanced visible-light photocatalytic activity. *Appl. Catal. B Environ* **204**, 304–315 (2017). <https://doi.org/10.1016/j.apcatb.2016.11.037>
  34. Q. Shi, C. Zhu, M.H. Engelhard, D. Du, Y. Lin, Highly uniform distribution of Pt nanoparticles on N-doped hollow carbon spheres with enhanced durability for oxygen reduction reaction. *RSC Adv* **7**(11), 6303–6308 (2017). <https://doi.org/10.1039/C6RA25391A>
  35. S.H. Lee, Y.G. Jeong, Y.I. Yoon, W.H. Park, Hydrolysis of oxidized polyacrylonitrile nanofibrous webs and selective adsorption of harmful heavy metal ions. *Polym. Degrad. Stab* **143**, 207–213 (2017). <https://doi.org/10.1016/j.polymdegradstab.2017.07.017>
  36. F. Huang, Y. Xu, S. Liao, D. Yang, Y.-L. Hsieh, Q. Wei, Preparation of amidoxime polyacrylonitrile chelating nanofibers and their application for adsorption of metal ions. *Materials* **6**(3), 969–980 (2013). <https://doi.org/10.3390/ma6030969>
  37. P. Kampalanonwat, P. Supaphol, The study of competitive adsorption of heavy metal ions from aqueous solution by aminated polyacrylonitrile nanofiber mats. *Energy Procedia* **56**, 142–151 (2014). <https://doi.org/10.1016/j.egypro.2014.07.142>
  38. D.M. Piper, T.A. Yersak, S.B. Son, S.C. Kim, C.S. Kang, K.H. Oh, C. Ban, A.C. Dillon, S.H. Lee, Conformal coatings of cyclized-PAN for mechanically resilient si nano-composite anodes. *Adv. Energy Mater* **3**(6), 697–702 (2013). <https://doi.org/10.1002/aenm.201200850>
  39. D. Wang, H. Dong, H. Zhang, Y. Zhang, Y. Xu, C. Zhao, Y. Sun, N. Zhou, Enabling a high performance of mesoporous  $\alpha$ -Fe<sub>2</sub>O<sub>3</sub> anodes by building a conformal coating of cyclized-pan network. *ACS Appl. Mater. Interfaces* **8**(30), 19524–19532 (2016). <https://doi.org/10.1021/acsami.6b06096>
  40. T. Gao, B. Wang, F. Wang, R. Li, L. Wang, D. Wang, LiAlCl<sub>4</sub>·3SO<sub>2</sub>: a promising inorganic electrolyte for stable Li metal anode at room and low temperature. *Ionics* **25**(9), 4137–4147 (2019). <https://doi.org/10.1007/s11581-019-02994-7>
  41. C.W. Park, S.M. Oh, Performances of Li/Li<sub>x</sub>CoO<sub>2</sub> cells in LiAlCl<sub>4</sub>·3SO<sub>2</sub> electrolyte. *J. Power Sources* **68**(2), 338–343 (1997). [https://doi.org/10.1016/S0378-7753\(97\)02518-4](https://doi.org/10.1016/S0378-7753(97)02518-4)

## Publisher's Note

Springer Nature remains neutral with regard to jurisdictional claims in published maps and institutional affiliations.

**Submit your manuscript to a SpringerOpen<sup>®</sup> journal and benefit from:**

- Convenient online submission
- Rigorous peer review
- Open access: articles freely available online
- High visibility within the field
- Retaining the copyright to your article

Submit your next manuscript at ► [springeropen.com](https://www.springeropen.com)